Journal of Non-Newtonian Fluid Mechanics 314 (2023) 105003

Contents lists available at ScienceDirect

Journal of Non-Newtonian Fluid Mechanics

journal homepage: www.elsevier.com/locate/jnnfm

Dynamics of a Taylor bubble through a shear-thinning fluid up to finite capillary numbers

Andrea Aquino, Davide Picchi *, Pietro Poesio

Department of Mechanical and Industrial Engineering, University of Brescia, Brescia 25123, Italy

ARTICLE INFO

Keywords:
Shear-thinning fluid
Taylor bubble
Multiphase
CFD

ABSTRACT

Although the motion of confined Taylor bubbles through non-Newtonian fluids is typical of many engineering and biological systems, a fundamental understanding of the problem is still an open problem. In this work, we investigate the dynamics of Taylor bubbles which move in an inelastic shear-thinning fluid that obeys the Carreau-Yasuda viscosity model by means of numerical simulations. We focus on regimes where inertia and buoyancy are negligible to assess the effect of the fluid rheology on bubble characteristics up to finite capillary numbers. First, we validate the recent lubrication theory by Picchi et al. (2021) by analysis of the trends of the film thickness and bubble speed in the small capillary number limit. Then, we show the existence of a general scaling that embeds for both zero-shear-rate and shear-thinning effects and holds up to finite capillary numbers. Interestingly, the shape of the Taylor bubble is strongly influenced by fluid rheology, which competes with the capillary number. Finally, the analysis of the viscosity fields shows an interplay between the zero-shear rate and shear thinning effects in different regions of the bubble, including the presence of recirculating vortexes that form ahead and behind the bubble.

1. Introduction

The motion of elongated Taylor bubbles in micro-channels is frequently encountered in many industrial processes, such as small-scale reactors, coating processes, and microfluidic devices [e.g., 1–4]. In medicine, it is crucial for the design of modern targeted microbubbles for drug delivery [e.g., 5] or understanding lung activity [e.g., 6] and air embolism [e.g., 7,8].

In these contexts, viscous forces and surface tension dominate over buoyancy and inertia, and the bubbles assume a symmetrical bullet shape. Since the seminal works of Fairbrother and Stubbs [9], Taylor [10], and Bretherton [11], researchers have primarily focused their attention on understanding the hydrodynamics of Taylor bubbles that moves through Newtonian fluids. More recent works investigate the effect of finite capillary number, inertia, and surface tension, [see e.g., 12–17].

However, in many applications, the fluids exhibit a non-Newtonian behavior. Biological solutions, emulsions, and polymers behave like shear-thinning fluids and their effective viscosity is a function of the imposed shear rate. Specifically, at low shear rates, the Newtonian effect dominates and the viscosity approaches the zero-shear-rate value. At higher shear rates, the shear-thinning effect dominates and the viscosity follows a power-law behavior, see Bird et al. [18]. Although rheological models that capture these features are available in the literature (e.g., the Carreau-Yasuda [19,20], and the Ellis models [21]), most of the efforts in studying Taylor bubbles often ignore those limiting behaviors, Kamişli and Ryan [22], Kamişli and Ryan [23], de Sousa et al. [24], Thompson et al. [25], Kawahara et al. [26], Fatehifar et al. [27] and Zhao et al. [28]. In fact, using the power-law viscosity model may lead to nonphysical results in the multiphase flow scenario since, at low shear rates, the viscosity is unbounded, (see e.g., Picchi et al. [29,30]).

Only recently, few attempts have been made to provide a consistent representation of bubble characteristics, which embeds both the low- and high shear-rate behaviors. Hewson et al. [31] noticed that using the Ellis viscosity model in a lubrication approximation tackled some of the inconsistencies generated by the power-law model. Picchi et al. [32] generalized Bretherton's theory to shear-thinning fluids (described by the Ellis viscosity model) and provided the scaling laws for the film thickness and the bubble speed as a function of the fluid rheology. Specifically, in the limit of small capillary numbers, the two-third scaling law for the film thickness still applies to shear-thinning fluids when the capillary number is based on the generalized effective viscosity. This new theory, however, has not been validated yet with experimental or numerical data. Up to now, numerical simulations of Taylor bubbles moving into realistic shear-thinning fluids are limited to the works of Moreira et al. [33] and Sontti and Atta [34]. Without a

* Corresponding author.
E-mail addresses: andrea.aquino@unibs.it (A. Aquino), davide.picchi@unibs.it (D. Picchi), pietro.poesio@unibs.it (P. Poesio).

https://doi.org/10.1016/j.jnnfm.2023.105003
Received 28 August 2022; Received in revised form 24 January 2023; Accepted 30 January 2023
Available online 2 February 2023

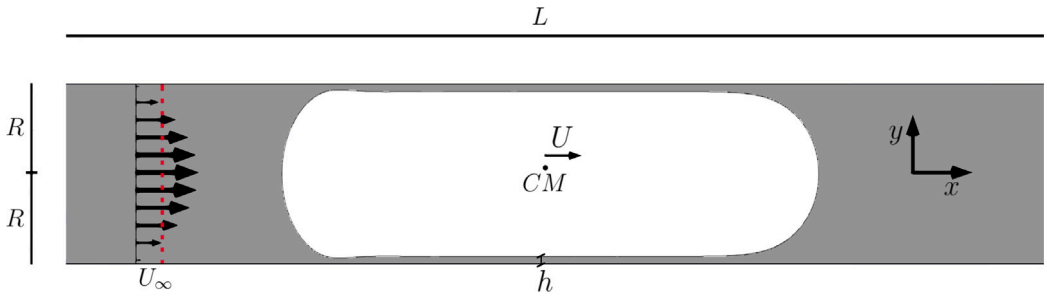

Fig. 1. Sketch of a Taylor bubble (white) moving in the shear-thinning liquid (gray); U_∞ is the average flow velocity far from the bubble; h is the uniform film thickness; the bubble is moving at speed U measured in the center of mass CM.

consistent set of experiments or simulations, it is not possible to prove or disprove the theoretical predictions of Picchi et al. [32]. In addition, the scaling laws obtained by Picchi et al. [32] are expected to hold only in the low capillary number limit and, the effect of finite capillary numbers is still unknown in this context.

To fill those gaps, in this work, we aim at assessing the role of fluid rheology and the capillary number on the bubble characteristics (e.g., film thickness, bubble speed, bubble shape) by numerical simulations. We simulate the Taylor bubble moving in a planar microchannel through a shear-thinning fluid whose viscosity is described by a simplified Carreau-Yasuda model. First, we validate the recent theory by Picchi et al. [32] by analysis of the trends of the film thickness, the bubble speed, and the bubble shape in the small capillary number limit. Then, we investigate the bubble hydrodynamics far from the validity range of the theory to understand the impact of finite capillary numbers on the problem. By analysis of the viscosity field, we also explain the interplay of zero-shear rates and shear thinning effects in different regions of the bubble, including the presence of recirculating vortexes ahead and behind the bubble.

2. Numerical simulations

2.1. Problem description

We study a Taylor bubble moving through an inelastic shear-thinning fluid in a planar microchannel of width $2R$, see Fig. 1. Far from the bubble, the fluid moves with average velocity U_∞ and, once it reaches the steady-state, the bubble moves at speed U. The bubble is sufficiently long so that a region with uniform film thickness, h, exists. To ensure the existence of the uniform film region, we consider bubbles of length $L_b \approx 8R$ above the threshold ($L_b = 5R$) suggested in Magnini et al. [16]. The effect of gravity is neglected.

Concerning the working fluids, the gas is assumed to be Newtonian, while the liquid viscosity is described by the Carreau-Yasuda model

$$\mu = \mu_\infty + (\mu_0 - \mu_\infty)[1 + (\lambda\dot{\gamma})^a]^{\frac{n-1}{a}}, \tag{1}$$

where $\dot{\gamma}$, μ_0, and μ_∞ are the magnitude of the shear-rate tensor, the viscosity at zero and infinite shear rate, respectively. The parameter λ is a constant that controls the onset of the shear-thinning behavior (at high values of λ, the shear-thinning behavior is shifted to lower shear rates) while the index n controls the degree of shear-thinning (for shear-thinning fluids $n < 1$). The dimensionless parameter a is positive and also describes the transition between the zero-shear-rate and the shear-thinning regions.

Although the Carreau-Yasuda model describes well the viscosity of many polymers and aqueous solutions, we will restrict our attention to fluids where the infinite-shear-rate viscosity is quite small compared to the zero-shear-rate viscosity, i.e., $\mu_\infty \ll \mu_0$. This condition is satisfied in many concentrated polymer solutions as shown in Bird et al. [18],Sousa et al. [35]. In addition to that, we will consider a simplified version of the Carreau-Yasuda model assuming that the parameter $a(n)$ is a function of the shear thinning index in order to match with the Ellis viscosity model, see Appendix A. This choice does not imply any loss of generality and has been primarily motivated by the comparison with the theory by Picchi et al. [32].

2.2. Governing equations and numerical simulations

In this work, we perform numerical simulations using the VOF solver `interFlow` of OpenFOAM-v1812, see Scheufler and Roenby [36]. The motion of the Taylor bubble in a shear-thinning fluid is obtained by solving the Navier–Stokes equations for the flow of two immiscible phases, i.e., a Newtonian and a non-Newtonian fluids, respectively. Both phases are assumed to be incompressible and are treated as a mixture with variable properties across the interface, see Tryggvason et al. [37]. Therefore, the governing equations for mass and momentum read

$$\nabla \cdot \boldsymbol{u} = 0, \tag{2}$$

$$\frac{\partial}{\partial t}(\rho_m \boldsymbol{u}) + \nabla \cdot (\rho_m \boldsymbol{u}\boldsymbol{u}) = -\nabla p + \nabla \cdot \boldsymbol{\tau} + \boldsymbol{F}_\sigma, \tag{3}$$

where $\boldsymbol{u} = (u_x, u_y)$ is the velocity vector, p is the pressure, $\boldsymbol{\tau} = \mu_m[\nabla \boldsymbol{u} + \nabla \boldsymbol{u}^T]$ is the stress tensor, and $\boldsymbol{F}_\sigma$ is the surface tension force vector; gravity is neglected in this work.

In the fluid domain a volume fraction field α identifies the occupation of the two phases. Specifically, α takes values of 1 in the computational cells occupied by the non-Newtonian fluid, 0 in the Newtonian bubble, and $0 < \alpha < 1$ in the bubble–fluid interface. The evolution of the volume fraction is described by the following advection equation

$$\frac{\partial \alpha}{\partial t} + \nabla \cdot (\alpha \boldsymbol{u}) = 0, \tag{4}$$

and the properties of the mixture are computed as

$$\rho_m = \rho_b + (\rho - \rho_b)\alpha, \quad \text{and} \quad \mu_m = \mu_b + (\mu - \mu_b)\alpha, \tag{5}$$

where ρ_b and μ_b are the bubble density and viscosity, respectively. The non-Newtonian fluid has a constant density, ρ, and its viscosity is given by Eq. (1). The surface tension force $\boldsymbol{F}_\sigma$ is included in Eq. (3) as a body force using the Continuum Surface Force (CSF) method [38] and the interface is reconstructed with the approach described in Scheufler and Roenby [36]. Such algorithm has been proven to be more effective in reducing the parasitic currents compared to previous approaches [see 36,39]. To further reduce the effects of spurious currents, the time step is constrained as suggested by Brackbill et al. [40].

Concerning the numerical set up, we used the Crank–Nicolson time scheme, Lee [41], and the convection terms are discretized by the Gaussian integration with linear interpolation (second-order schemes in space and time) as in Silva et al. [42]. The VanLeer limiter [43] guarantees that the volume fraction remains bounded and we kept the Courant number below 0.3. Each simulation is initialized by placing a bubble of volume V in the computational domain. The motion of the Taylor bubble is driven by the flow imposed at the entrance of the

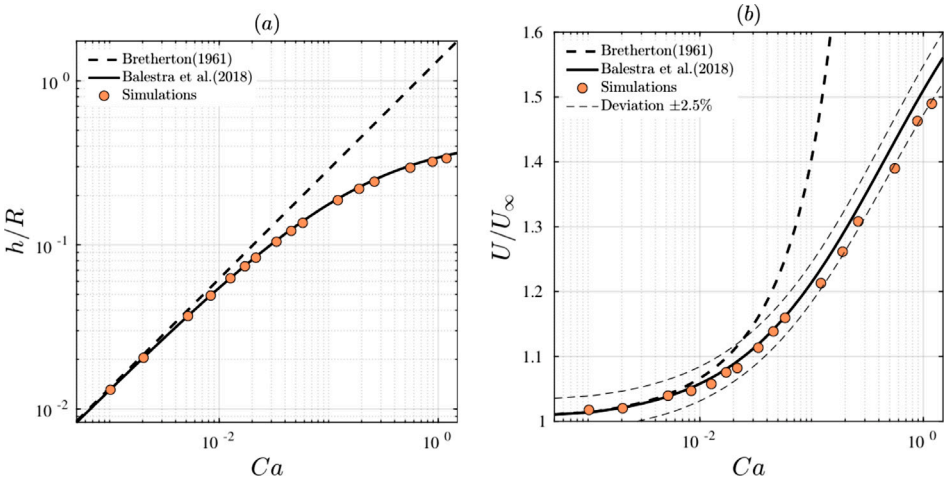

Fig. 2. Validation of the dimensionless film thickness, h/R, and relative bubble speed, U/U_∞, in the Newtonian case.

channel (with average velocity U_∞, see Fig. 1). The no-slip condition is imposed at the channel wall while the outlet is set as a zero-gradient boundary [44]. The simulation ends when the bubble reaches the steady state.

2.2.1. Computational grid

The computational domain is made of uniform square cells, which are gradually refined at the wall boundary in order to accurately capture the near-wall film dynamics. This refinement ensures that the hydrodynamics of the film region is properly described, in particular at low capillary numbers, as shown by Hoang et al. [44] and Magnini et al. [16]. Aimed at identifying the parameters of the simulations, a grid test has been conducted following the strategy described by Magnini et al. [16]. The idea is to progressively refine the mesh in the vertical direction observing the evolution of the main integral variables (i.e., the film thickness) with respect to the number of computational cells. The mesh is chosen identifying when the film thickness deviated by less than 0.5% from those measured with more refined meshes in the most severe case, i.e., the case with the lowest capillary number investigated. We found that a mesh including 130 square cells of uniform size along the vertical direction, followed by 15 gradually refined mesh elements near each of the two walls satisfies the grid check procedure given by Magnini et al. [16].

2.3. Parameter space and governing dimensionless numbers

In this work, we are interested only in regimes where viscous forces and surface tension dominate over buoyancy and inertia. To guarantee that, we neglect gravity so that the macroscopic Bond number is identically zero, and we look at conditions in which the bubble density, ρ_b, and viscosity, μ_b, are negligible when compared to liquid density, ρ, and the zero-shear-rate viscosity, μ_0, namely $\mu_b/\mu_0 = 10^{-2}$ and $\rho_b/\rho = 10^{-3}$. Also, the macroscopic Reynolds number (based on the channel half-size R, the average velocity of the fluid far from the bubble, U_∞, and the zero-shear-rate viscosity, μ_0) is kept constant as $Re = \rho U_\infty R/\mu_0 = 1$.

The simulations are conducted spanning a wide range of capillary numbers

$$Ca_\infty = \frac{\mu_0 U_\infty}{\sigma} \quad \in [10^{-3};\ 1], \tag{6}$$

where σ is the surface tension. Specifically, Ca_∞ is changed by varying the surface tension, and, once at the steady state, the corresponding capillary number based on the bubble speed is calculated

$$Ca = \frac{\mu_0 U}{\sigma}. \tag{7}$$

The effect of the rheology is studied with respect to few dimensionless parameters. Specifically, if we choose the zero-shear-rate viscosity, μ_0, the bubble speed, U, and the uniform film thickness, h, as the characteristic scales for liquid viscosity, the velocity, and the spatial variable, we can make Eq. (1) dimensionless as

$$\frac{\mu}{\mu_0} = \frac{\mu_\infty}{\mu_0} + \left(1 - \frac{\mu_\infty}{\mu_0}\right)\left[1 + (Cu\dot{\gamma})^a\right]^{\frac{n-1}{a}}, \tag{8}$$

where $\dot{\gamma}$ is the dimensionless shear rate and Cu is the Carreau number defined as

$$Cu = \frac{\lambda U}{h}. \tag{9}$$

As mentioned earlier, we neglect the effect of the infinity-shear-rate viscosity by assuming that $\mu_\infty/\mu_0 = 0$. then, when $Cu \to 0$, the effective viscosity reduces to the Newtonian limit, while for $Cu \to \infty$, the shear-thinning effect dominates and the viscosity matches that of a power-law fluid, i.e., $\mu/\mu_0 \sim \dot{\gamma}^{n-1}$.

Since both h and U are unknown before running the simulation, we span a range of Carreau numbers based on the average velocity of the fluid far from the bubble U_∞ and the uniform film thickness in the small capillary number limit h_0

$$Cu^0_\infty = \frac{\lambda U_\infty}{h_0} \quad \in [10^{-2};\ 1.2], \tag{10}$$

where h_0 is obtained from the scaling law by Picchi et al. [32].

2.4. Validation

We validated the numerical setup by comparing the dimensionless film-thickness, h/R, and the bubble speed ratio, U/U_∞, against the correlation proposed by Balestra et al. [45]. Such correlation is an extension of the Aussillous and Quéré [12] correlation and it has been proven to be very accurate in the case of Newtonian fluids up to finite Ca. As shown in Fig. 2(a), the simulations agree well with the model for the dimensionless film thickness in the entire range of capillary numbers, while, concerning the bubble speed ratio, there is a deviations about 2.5% at the highest capillary numbers, see Fig. 2(b). As expected, the simulations follow the 2/3 scaling law proposed by Bretherton [11] at low Ca. Also, the bubble shape and the recirculating pattern agree with the ones presented in Balestra et al. [45].

3. Results and discussion

3.1. Lubrication film

In this Section, we discuss the impact of fluid rheology and the capillary number on the uniform film thickness.

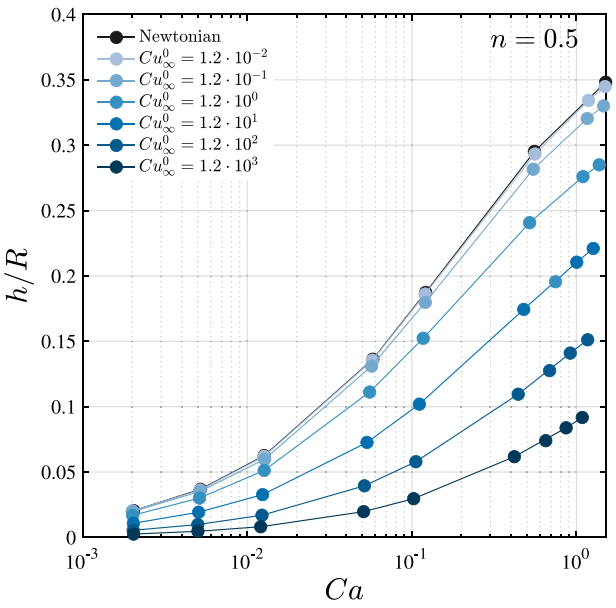

Fig. 3. Uniform film thickness as a function of the capillary number Ca and the Carreau number Cu^0_∞ for $n = 0.5$ and $a = 0.841$.

In Fig. 3 we present the evolution of h/R with respect to the capillary number, Ca, and the Carreau number, Cu^0_∞, defined in Eqs. (7) and (10), respectively. When Cu^0_∞ is small, the film thickness collapse over the Newtonian limit. At higher Carreau numbers, instead, h/R decreases since the shear-thinning effect become important. We explain this behavior with a reduction of the effective viscosity that diminishes the effective capillary number (this aspect will be discussed in detail later on). Also, the film thickness increases with Ca: the bubble forms a thinner film compared to a Newtonian fluid with the same capillary number, see Fig. 3.

Differently from the Newtonian case, where the film thickness is determined uniquely by the capillary number (when inertia and buoyancy are negligible, see Aussillous and Quéré [12]), inspection of Eq. (8) suggests that the film thickness for shear-thinning fluids is determined by the interplay of five dimensionless, i.e., $h/R = f(Ca, Cu, n, a, \mu_\infty/\mu_0)$ where Cu is the Carreau number based on the bubble speed and the film thickness as defined in Eq. (9). Here, due to the simplifications on the rheological model discussed in Section 2.1, the film thickness will depend only on the capillary number, the Carreau number, the shear-thinning index, and the parameter a (which is a function of n as discussed in Appendix A), i.e., $h/R = f(Ca, Cu, n, a(n))$.

Aimed at finding a consistent scaling law for the film thickness, we propose an empirical model inspired by the work of Aussillous and Quéré [12]. This choice is motivated by the fact that such model captures well the effect of finite capillary numbers on the film thickness in the case of Newtonian fluids. Here, we adapt the Aussillous and Quéré [12] scaling law as follows

$$\frac{h}{R} = \frac{P(3Ca)^{2/3}}{1 + PQ(3Ca)^{2/3}}, \tag{11}$$

where both $P(Cu, n, a)$ and $Q(Cu, n, a)$ are functions of the fluid rheology. The fitting functions incorporate both the zero-shear-rate and the shear-thinning effects and are given by

$$P = 0.643 \left[1 + (\beta Cu)^a\right]^{\frac{2(n-1)}{3a}}, \tag{12}$$

$$Q = 2.32 + \delta Cu^\theta, \tag{13}$$

where β, δ, and θ are fitting parameters while $a(n)$ is computed accordingly to Appendix A. Such coefficients are designed in such a way that, in the Newtonian limit (for $Cu \to 0$), $P = 0.643$ and $Q \approx 2.32$, in accordance with Aussillous and Quéré [12] and Balestra et al. [45]. The fitting functions have been found by fitting Eqs. (12) and (13) on data presented in Fig. 3 using non linear regression. Specifically, we use the tool *nlinfit* of Matlab which finds the fitting parameters though the Iteratively Reweighted Least Squares method, see Holland and Welsch [46]. The evolution of P and Q with respect to Cu is shown in Fig. 4 for the case with $n = 0.5$ and $a = 0.841$.

For the sake of physical interpretation, it should be remarked that the model for the film thickness, Eq. (11), is still based on the definition of the capillary number defined with the zero-shear-rate viscosity, see Eq. (7). It would be desirable to recast the model embedding both the zero-shear-rate and the shear-thinning effects. To this aim, we define an effective capillary number

$$Ca_e = \frac{\mu_e U}{\sigma}, \tag{14}$$

where the effective viscosity μ_e is a function of the coefficient $P(Cu, n, a)$

$$\mu_e = \mu_0 \left(\frac{P}{0.643}\right)^{3/2}. \tag{15}$$

Fig. 5(a) shows a plot of the effective viscosity as a function of the Carreau number, which can be seen as an effective shear-rate for the problem. In fact, μ_e reduces to the zero-shear-rate viscosity when $Cu \to 0$ and it matches that of a power-law fluid for $Cu \to \infty$. In other words, as the shear thinning effect becomes dominant, the effective viscosity diminishes reducing the effective capillary number of the problem. Inspired by the work of Picchi et al. [32], the effective viscosity can be described by the following law

$$\frac{\mu_e}{\mu_0} = \begin{cases} 1, & \text{if} \quad Cu \to 0, \\ 0.136(17 - 12n)Cu^{(1-n)}, & \text{if} \quad Cu \to \infty. \end{cases} \tag{16}$$

Note that, for $Cu \to \infty$, the effective viscosity approaches the power-law limit of Eq. (8)

$$\mu \sim \kappa Cu^{1-n}, \tag{17}$$

where $\kappa = 0.136(17 - 12n)$.

Substituting the Eqs. (14) and (15) into Eq. (11) yields to a generalized model for the film thickness

$$\frac{h}{R} = \frac{0.643\,(3Ca_e)^{2/3}}{1 + 0.643\,Q\,(3Ca_e)^{2/3}}, \tag{18}$$

where $Q(Cu, n, a)$ is given in Eq. (13). Specifically, the functional dependence of the Aussillous and Quéré [12]'s model is preserved in the case of shear-thinning fluids if the model is formulated in terms of the effective capillary number. The only difference with respect to the Newtonian case lies in the definition of the effective viscosity, which is a function of the Carreau number, and the coefficient Q, which is also a function of the fluid rheology. When the capillary number is small, the dimensionless film thickness follows the classical 2/3 scaling behavior and Eq. (18) converges to the theory presented by Picchi et al. [32]

$$\frac{h}{R} \sim 0.643\,(3Ca_e)^{2/3} \quad \text{for} \quad Ca_e \to 0. \tag{19}$$

This scaling behavior is confirmed by our simulations in Fig. 5(b) and it holds approximately up to $Ca_e = \mathcal{O}(10^{-1})$. At higher Ca_e, instead, the film thickness saturates for increasing capillary numbers, similarly to what was observed in Taylor [10] and Aussillous and Quéré [12]. Interestingly, the film problem keeps the same scaling structures as the Newtonian one once rescaled in terms of the effective capillary number. The proposed model represents the generalization of the Aussillous and Quéré [12] correlations to shear-thinning fluids.

The results presented in this Section are limited to a shear-thinning index $n = 0.5$. However, it can be easily shown that the proposed framework also applies to cases when the shear-thinning index varies. Fig. 4 show the results for $n = 0.65$ and $a = 0.48$.

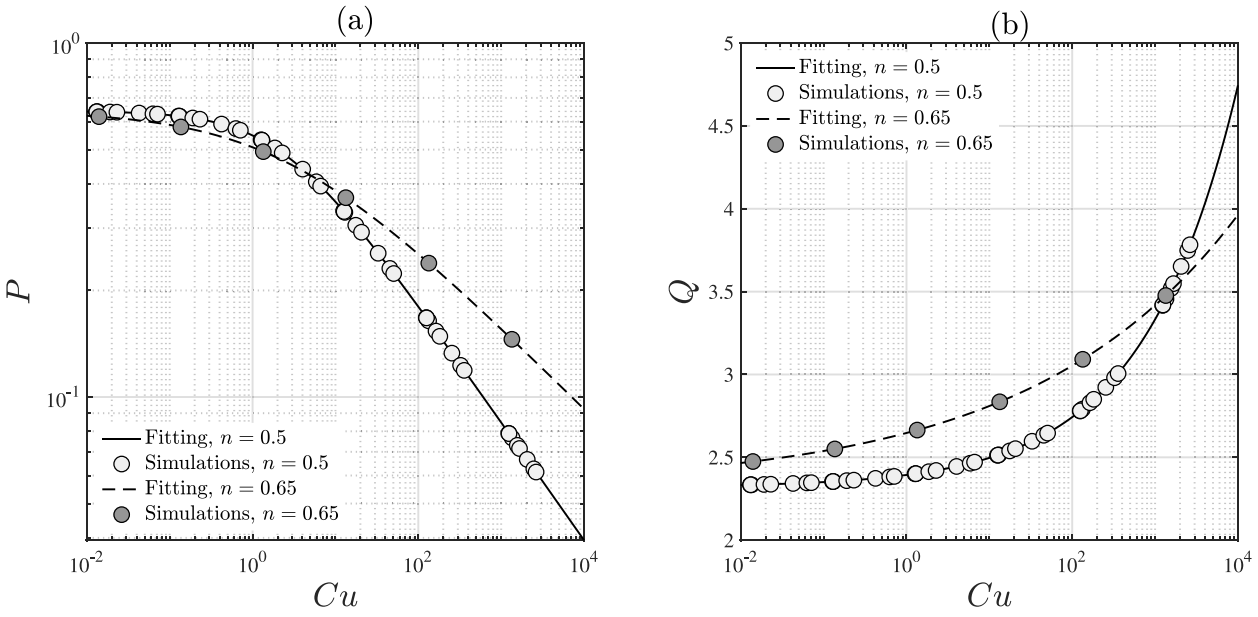

Fig. 4. Plot of the fitting functions (a) $P(Cu, n, a(n))$; (b) $Q(Cu, n, a(n))$. When $n = 0.5$, $a = 0.841$; when $n = 0.65$, $a = 0.48$.

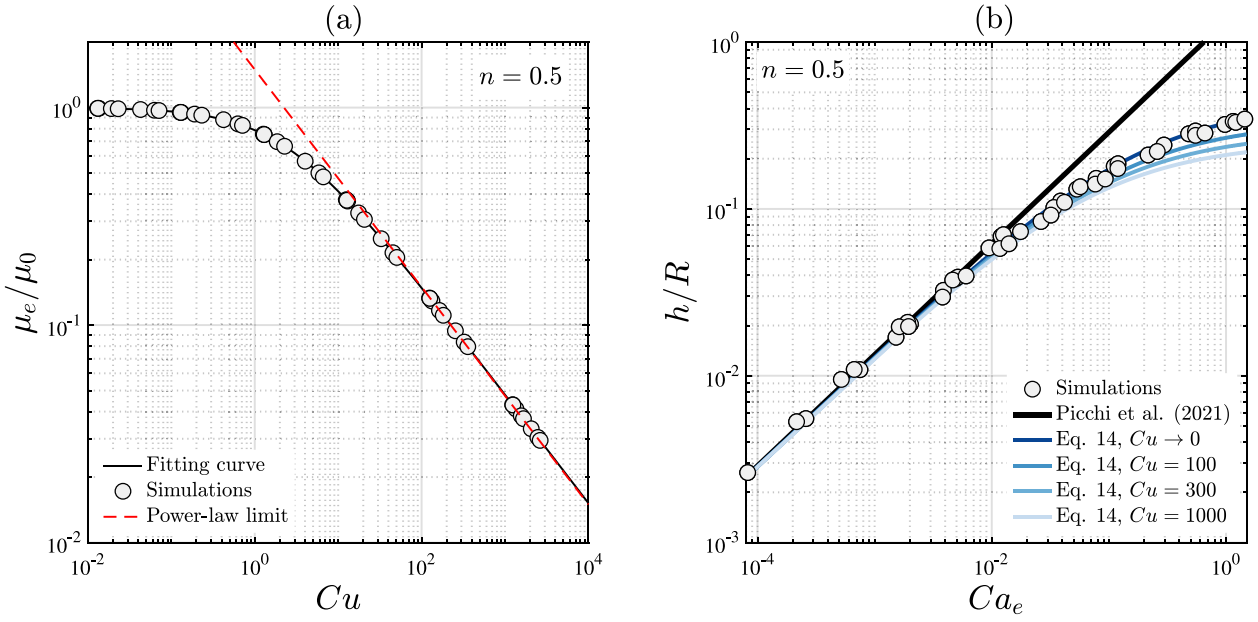

Fig. 5. (a) Effective viscosity as a function of Cu for $n = 0.5$ and $a = 0.841$; (b) dimensionless film thickness as a function of the generalized capillary number, Ca_e, and Cu for $n = 0.5$ and $a = 0.841$.

3.2. Bubble speed

The bubble speed U is a critical parameter in the design of many applications involving Taylor bubbles. Specifically, the ratio between the bubble speed, U, and the average velocity of the fluid ahead of the bubble, U_∞, is a function of the dimensionless film thickness only and it can be estimated from the mass balance (see Picchi et al. [32]) obtaining

$$\frac{U}{U_\infty} = \frac{1}{1 - h/R}. \tag{20}$$

Substituting Eq. (11) into Eq. (20), we get the following scaling law for the bubble speed

$$\frac{U}{U_\infty} = \frac{1 + QP(3Ca)^{2/3}}{1 + (Q-1)P(3Ca)^{2/3}}, \tag{21}$$

or, expressing the film thickness in terms of the effective capillary number, we obtain

$$\frac{U}{U_\infty} = \frac{1 + 0.643Q(3Ca_e)^{2/3}}{1 + 0.643(Q-1)(3Ca_e)^{2/3}}. \tag{22}$$

Fig. 6(a) shows the bubble speed obtained from the numerical simulations. The bubble always moves faster than the fluid ahead, namely $U/U_\infty > 1$ in all the ranges of Ca and Cu^0_∞. As expected, when the Carreau number is small, the bubble moves almost at the same speed as a Newtonian fluid with the same Ca. When the shear-thinning effect dominates, instead, the bubble flows slowly compared to a Newtonian bubble with the same capillary number Ca.

The evolution of the bubble speed ratio in the limit of $Ca \to 0$ is depicted in Fig. 6(b): the data are slightly below the theoretical

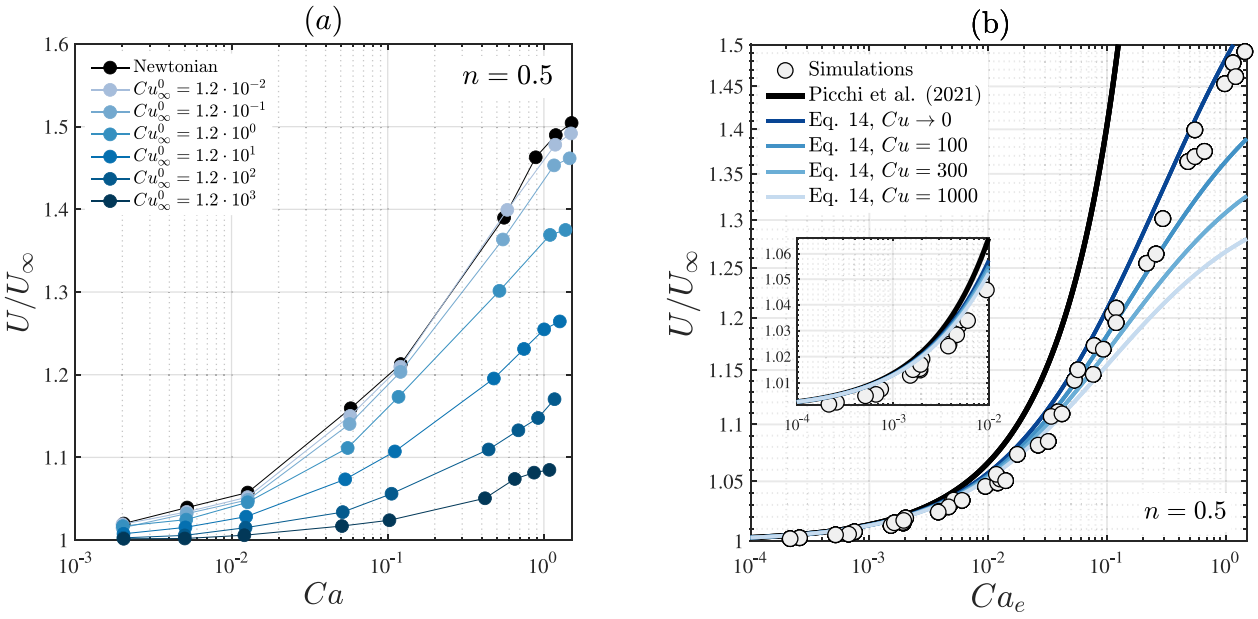

Fig. 6. (a) Bubble speed as a function of Ca for $n = 0.5$ and $a = 0.841$; (b) Bubble speed as a function of the effective capillary number Ca_e for $n = 0.5$ and $a = 0.841$.

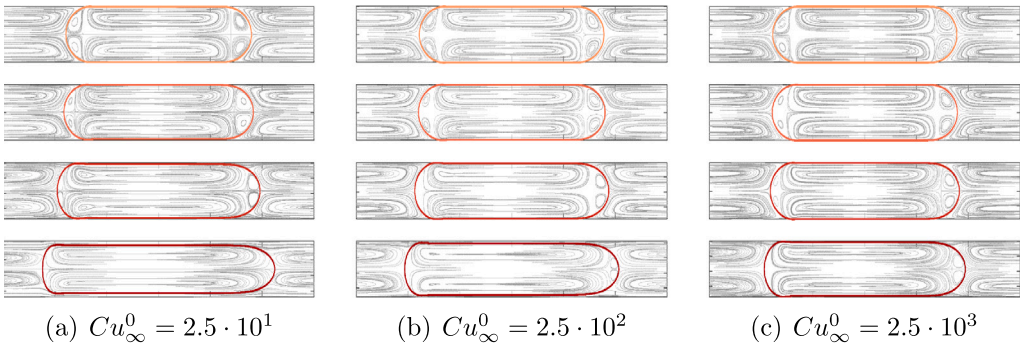

Fig. 7. Effect of capillary number and Cu^0_∞ on bubble profiles and flow streamlines in a reference frame attached to the bubble for $n = 0.5$ and $a = 0.841$. — $Ca_\infty = 1$; — $Ca_\infty = 0.1$; — $Ca_\infty = 0.01$; — $Ca_\infty = 0.002$. Bubbles are aligned with respect to the center of mass.

predictions by Picchi et al. [32]

$$\frac{U}{U_\infty} \sim \frac{1}{1 - 0.643\,(3Ca_e)^{2/3}} \quad \text{for} \quad Ca_e \to 0. \tag{23}$$

At finite Ca_e, the speed ratio saturates and the trend of numerical simulations is well captured by Eq. (22). Specifically, the lower the effective viscosity is (and the effective capillary number), the slower the bubble is. The little spread of the data is due to the fact that each simulations has a different Cu, as shown in Fig. 5(a).

3.3. Bubble shape and recirculation patterns

The bubble shape and recirculating flows ahead and behind the bubble are strongly affected by the capillary number and the fluid rheology. Specifically, when the capillary number is small, surface tension dominates over viscous forces and the Taylor bubble has a symmetrical shape, i.e., the main curvature in the front and in the rear is almost indistinguishable (see the first row in Fig. 7). As the capillary number increases, the uniform film thickness increases and the bubble assumes a bullet shape (see Fig. 7).

The effect of Ca_∞ on the bubble shape is summarized in Fig. 8. Increasing Ca_∞ results in a thicker film and, as a consequence, in longer bubbles. This effect is more pronounced when the Carreau number is small, Fig. 8(c). Instead, when the Carreau number is high and the shear-thinning effect dominates, changes in the bubble shape are mitigated due to the competition between a higher flow rate ahead of the bubble (which increases Ca) and the shear-thinning effect (which decreases the effective viscosity).

The degree of shear-thinning impact on the bubble shape via the Carreau number as shown in Fig. 9. Specifically, at low Cu^0_∞, the zero-shear-rate effect dominates and the bubble shape is practically indistinguishable from the Newtonian one. At high Cu^0_∞, the shear-thinning effect plays an important role: the uniform film becomes thinner and the bubble shrinks. In other words, increasing the degree of shear-thinning of the problem has the same effect of reducing the effective capillary number of the problem. This effect is evident at all the capillary numbers investigated in this work, see Fig. 9.

To summarize the effect of the capillary number and the fluid rheology on the bubble shape, we compute the dimensionless radius of curvature $(\kappa R)^{-1}$ at the bubble tip (κ is the dimensional curvature). The curvature is calculated by fitting an arc of a circle at the bubble tip. When the capillary number is small, the radius of curvature is well approximated by the channel radius, while, at higher capillary numbers, the film becomes thicker, and, therefore, the radius of curvature diminishes. Fig. 10(a) shows the evolution of the dimensionless radius with respect to the effective capillary number. Both the Newtonian and the shear-thinning data collapse well around the following master curve

$$(\kappa R)^{-1} = \left(1 + Ca_e^{1/2}\right)^{-1.863}, \tag{24}$$

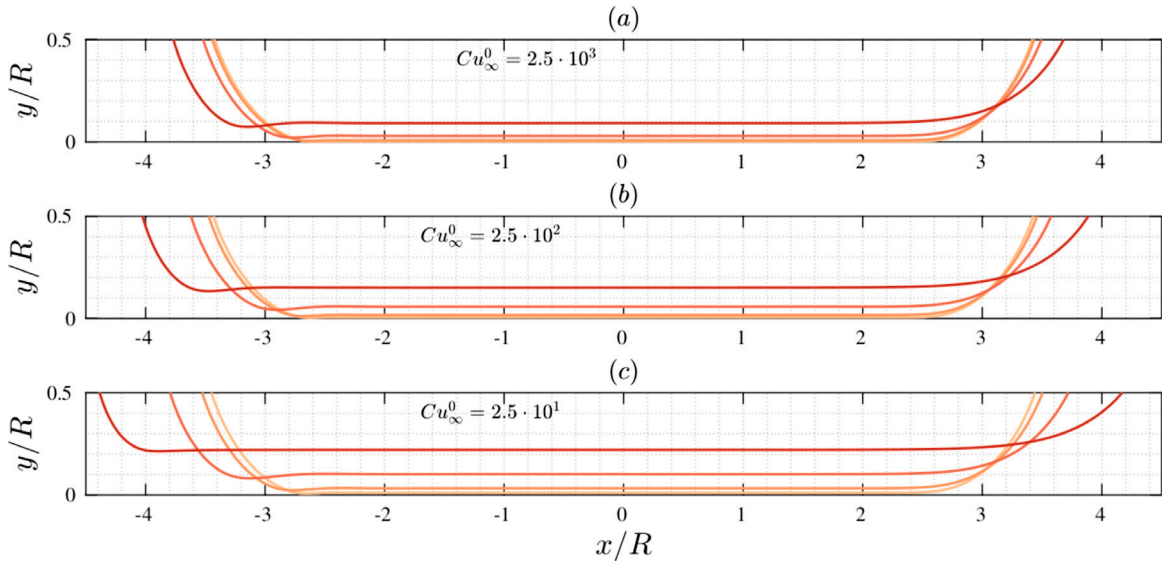

Fig. 8. Effect of capillary number, Ca_∞, at different Carreau number, Cu^0_∞, for $n = 0.5$ and $a = 0.841$. — $Ca_\infty = 0.002$; — $Ca_\infty = 0.01$; — $Ca_\infty = 0.1$; — $Ca_\infty = 1$.

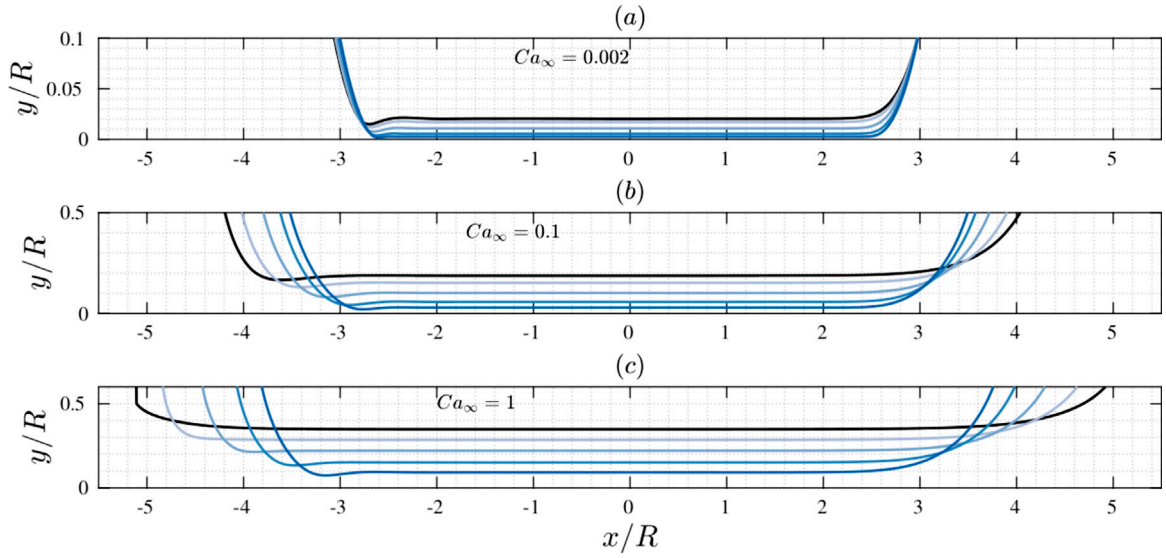

Fig. 9. Effect of the Carreau number, Cu^0_∞, at different capillary number, Ca_∞, for $n = 0.5$ and $a = 0.841$. The — is the Newtonian case, while Cu^0_∞ = —$2.5 \cdot 10^0$; —$2.5 \cdot 10^1$; —$2.5 \cdot 10^2$; —$2.5 \cdot 10^3$.

where the effect of the fluid rheology is embedded in the definition of the effective capillary number. This results shows that, at the bubble tip, a jump in pressure is maintained due to the interface curvature, as shown in Figs. B.17 and B.18. On the other hand, in the uniform film region where the interface is almost flat, the pressure field in the gas and the shear-thinning liquid is practically uniform.

From the streamlines in the shear-thinning liquid, we can analyze the characteristics of the recirculating patterns. The simulations where recirculating vortexes are present are mapped in Fig. 10(b) as a function of the dimensionless film thickness and the Carreau number based on the channel half-width and the fluid velocity ahead of the bubble, $Cu^R_\infty = \lambda U_\infty / R$. In this case, the vortexes form only when the maximal velocity ahead exceeds the bubble velocity. The few simulations where the vortexes are not detected are well predicted by the critical film-thickness for the appearance of the recirculating vortexes estimated by Picchi et al. [32], see Fig. 10(b). Since the theoretical model by Picchi et al. [32] is formulated in terms of the Ellis viscosity model and the current simulations are carried out using the Carreau viscosity model, we show how the two models can be interchanged in Appendix A. Note that the critical film thickness is a function of the fluid rheology: in the Newtonian limit (for $Cu^R_\infty \to 0$), $h_{crit}/R = 1/3$ while the shear-thinning effect reduces its value.

The dividing streamlines separate the circulating vortex ahead of the bubble (if present) and the liquid flowing towards the film. Following Picchi et al. [32], its location, y_d, can be determined through a mass balance in the moving reference frame between the region ahead of the bubble and the film region as

$$(0 - U)h = \int_0^{y_d} \left(u_\infty(y) - U\right) dy, \tag{25}$$

where $u_\infty(y)$ is the velocity profile in the liquid ahead of the bubble. Note that the net flow rate calculated over the vortex region is zero. Computing Eq. (25) on our simulations, we get the exact location of the dividing streamline, plotted in Fig. 11(a) in terms of the dimensionless variable $Y_d = y_d/R$. The data collapse well over the theoretical prediction obtained by Picchi et al. [32] when $h/R \ll 1$ (or $Ca_e \to 0$): the dividing streamlines scales with the dimensionless film thickness,

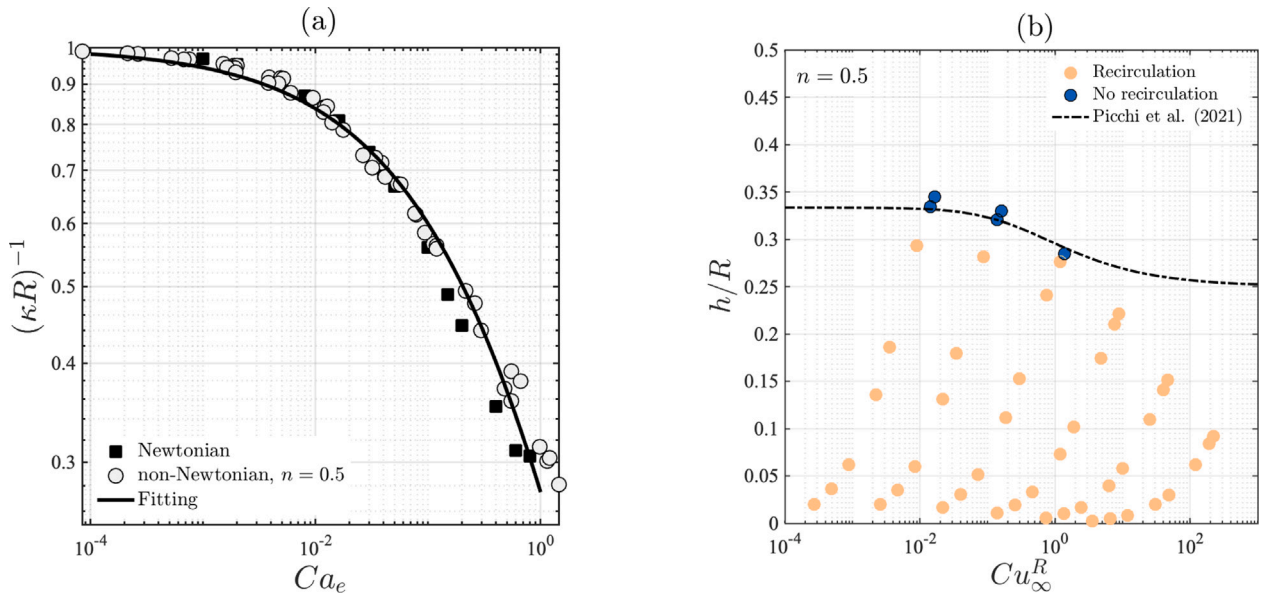

Fig. 10. (a) Dimensionless radius of curvature at the tip of the bubble front as a function of the effective capillary number for a Newtonian fluid and a shear-thinning fluid with $n = 0.5$ and $a = 0.841$. (b) Mapping of simulations where flow recirculation ahead of the bubble appears as a function of Cu_∞^R for $n = 0.5$ and $a = 0.841$. The critical film thickness for the appearance of the flow recirculation predicted by Picchi et al. [32] is also plotted.

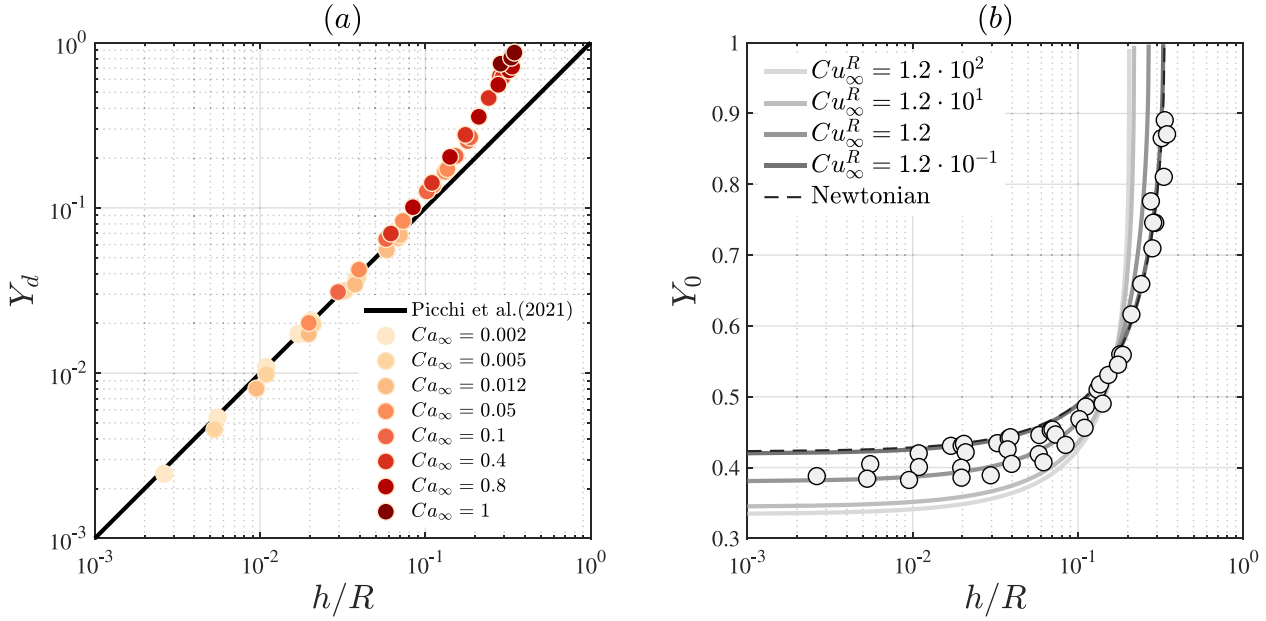

Fig. 11. (a) Location of the dividing streamline, $Y_d = y_d/R$, as a function of Ca_∞ for a shear-thinning fluid with $n = 0.5$ and $a = 0.841$. (b) Heights of the center of the recirculating vortexes, $Y_0 = y_0/R$, ahead of the bubble as a function of Cu_∞^R for $n = 0.5$ and $a = 0.841$. Lines are computed with the theory given by Picchi et al. [32].

$Y_d \sim h/R$ and slightly deviates from such behavior only when the capillary number is finite and film thickness is thicker than 0.1.

Also, the location of the center of the recirculating zone y_0 can be computed by looking for the point where the velocity in the liquid ahead equals the bubble velocity, see Picchi et al. [32]. Fig. 11(b) shows the location of the vortex center in terms of the dimensionless coordinate, $Y_0 = y_0/R$: as the film thickness, h/R, increases, the vortexes shifts closer to the channel axis. In fact, we do not expect the existence of the recirculating vortexes when h/R is bigger than the critical value plotted in Fig. 10(b). The comparison between our results and the model by Picchi et al. [32] is quite satisfactory in the range $Cu_\infty^R = [0.1, 120]$.

3.4. Viscosity field around the Taylor bubble

To better understand the impact of the shear-thinning effect on the bubble characteristics, we examine the viscosity field in the surroundings of the Taylor bubble. Fig. 12 shows the effective viscosity field and its value at the wall computed at the steady state in the small capillary limit, $Ca_\infty = 0.002$, as a function of the Carreau number. When the Carreau number is small, the fluid almost behaves like a Newtonian one and the shear-thinning effect is negligible over the entire meniscus, see Fig. 12(a). When the Carreau number increases, the shear-thinning effects dominate near the nose and the rear of the bubble (in proximity to the typical meniscus oscillations). There, the shear-rate presents local

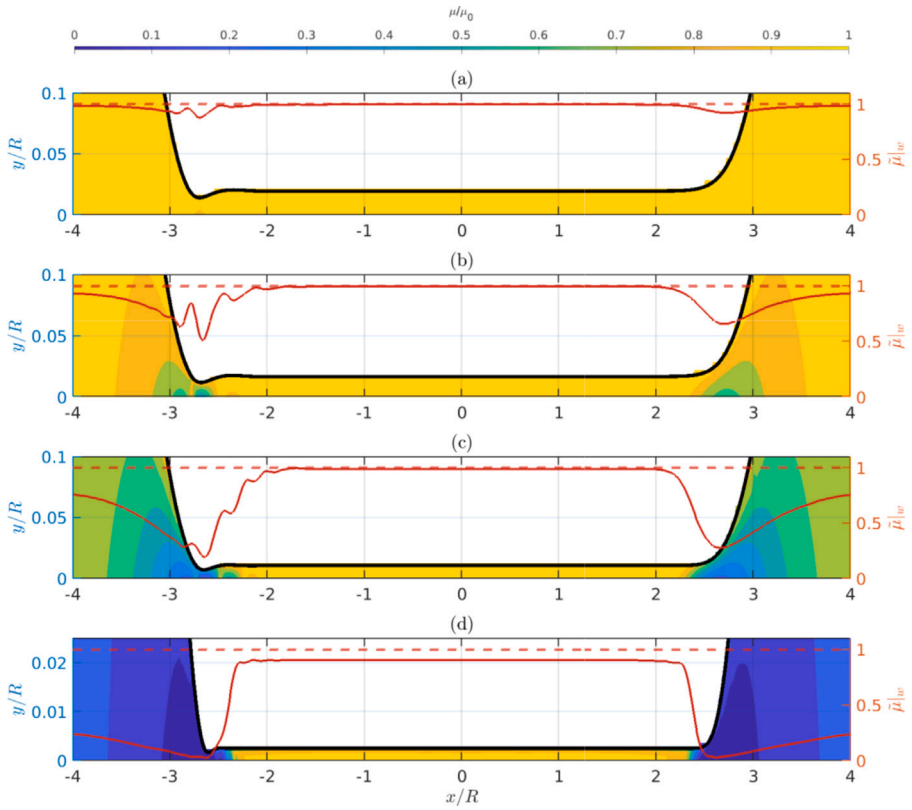

Fig. 12. The viscosity field in the shear-thinning liquid surrounding the bubble; the red line is the effective viscosity computed at wall (—); the dashed line represents the Newtonian limit (- -). In all cases $Ca_\infty = 0.002$, $n = 0.5$ and $a = 0.841$, while (a) $Cu^0_\infty = 2.5 \cdot 10^{-2}$, (b) $Cu^0_\infty = 2.5 \cdot 10^{-1}$, (c) $Cu^0_\infty = 2.5 \cdot 10^{0}$, (d) $Cu^0_\infty = 2.5 \cdot 10^{2}$.

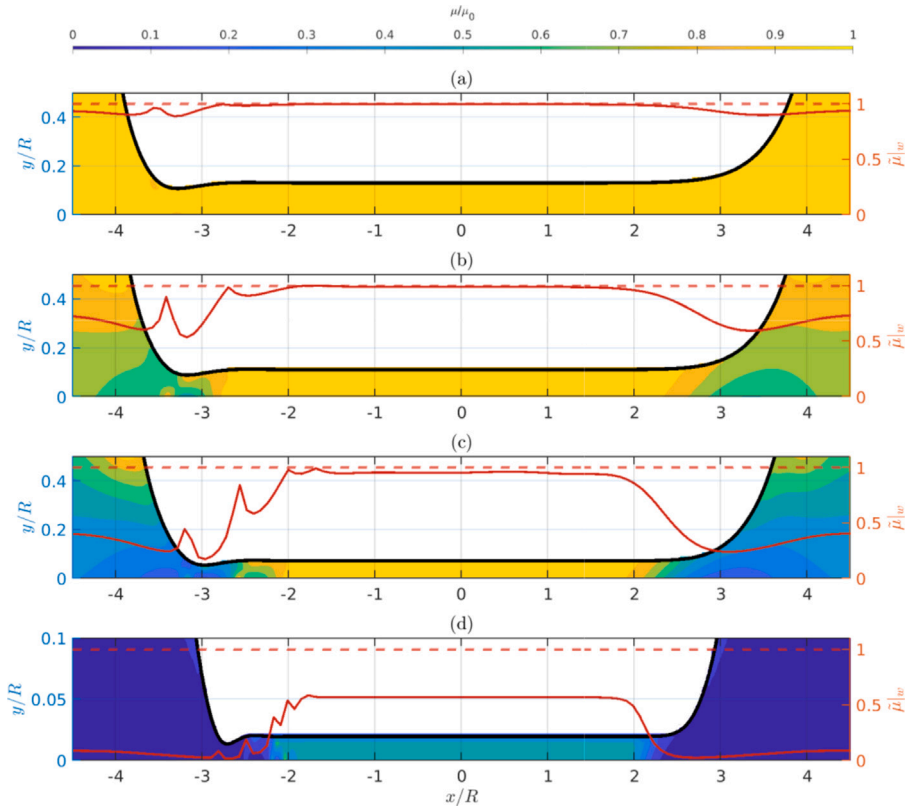

Fig. 13. The viscosity field in the shear-thinning liquid surrounding the bubble; the red line is the effective viscosity computed at wall (—); the dashed line represents the Newtonian limit (- -). In all cases $Ca_\infty = 0.05$, $n = 0.5$ and $a = 0.841$, while (a) $Cu^0_\infty = 2.5 \cdot 10^{-2}$, (b) $Cu^0_\infty = 2.5 \cdot 10^{-1}$, (c) $Cu^0_\infty = 2.5 \cdot 10^{0}$, (d) $Cu^0_\infty = 2.5 \cdot 10^{2}$.

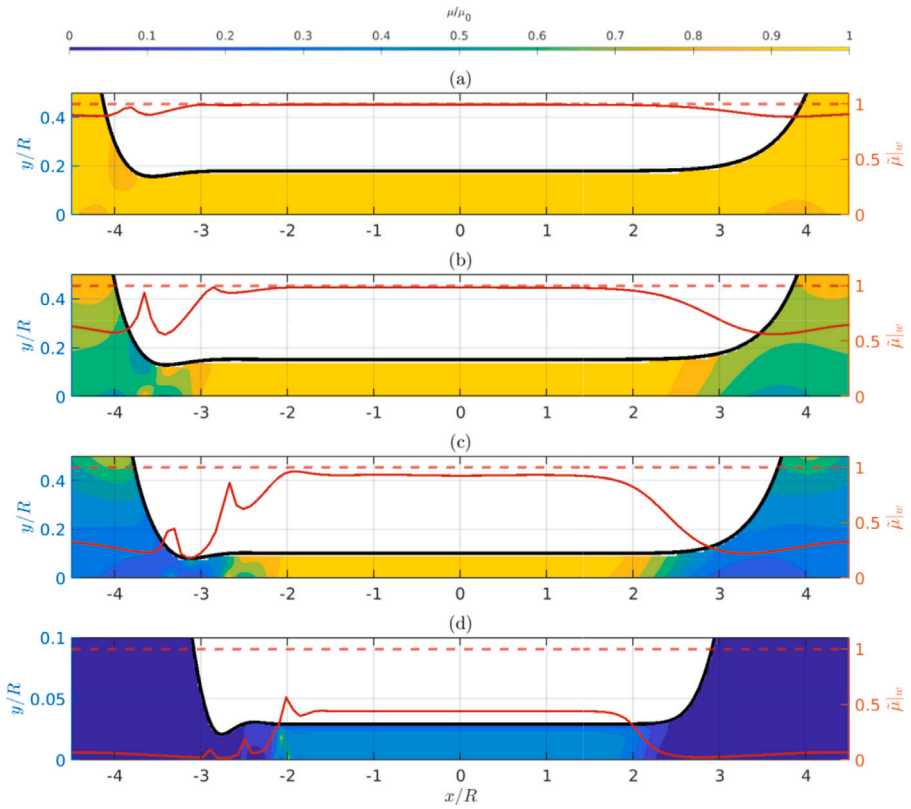

Fig. 14. The viscosity field in the shear-thinning liquid surrounding the bubble; the red line is the effective viscosity computed at wall (—); the dashed line represents the Newtonian limit (- -). In all cases $Ca_\infty = 0.1$, $n = 0.5$ and $a = 0.841$, while (a) $Cu^0_\infty = 2.5 \cdot 10^{-2}$, (b) $Cu^0_\infty = 2.5 \cdot 10^{-1}$, (c) $Cu^0_\infty = 2.5 \cdot 10^{0}$, (d) $Cu^0_\infty = 2.5 \cdot 10^{2}$.

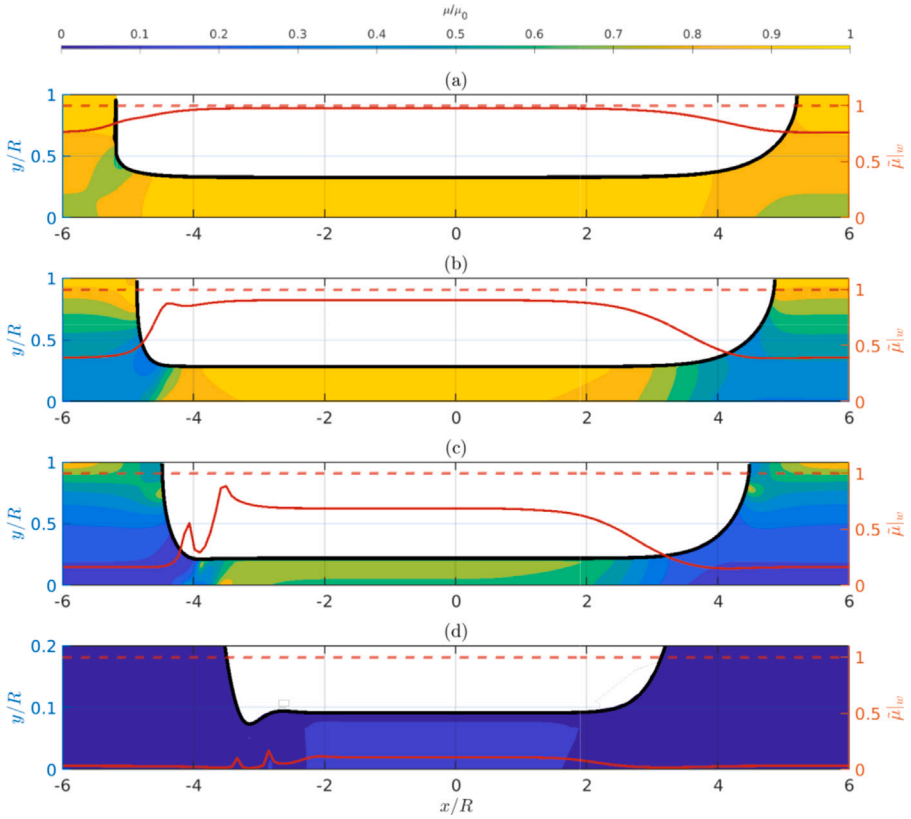

Fig. 15. The viscosity field in the shear-thinning liquid surrounding the bubble; the red line is the effective viscosity computed at wall (—); the dashed line represents the Newtonian limit (- -). In all cases $Ca_\infty = 1$, $n = 0.5$ and $a = 0.841$, while (a) $Cu^0_\infty = 2.5 \cdot 10^{-2}$, (b) $Cu^0_\infty = 2.5 \cdot 10^{-1}$, (c) $Cu^0_\infty = 2.5 \cdot 10^{0}$, (d) $Cu^0_\infty = 2.5 \cdot 10^{2}$.

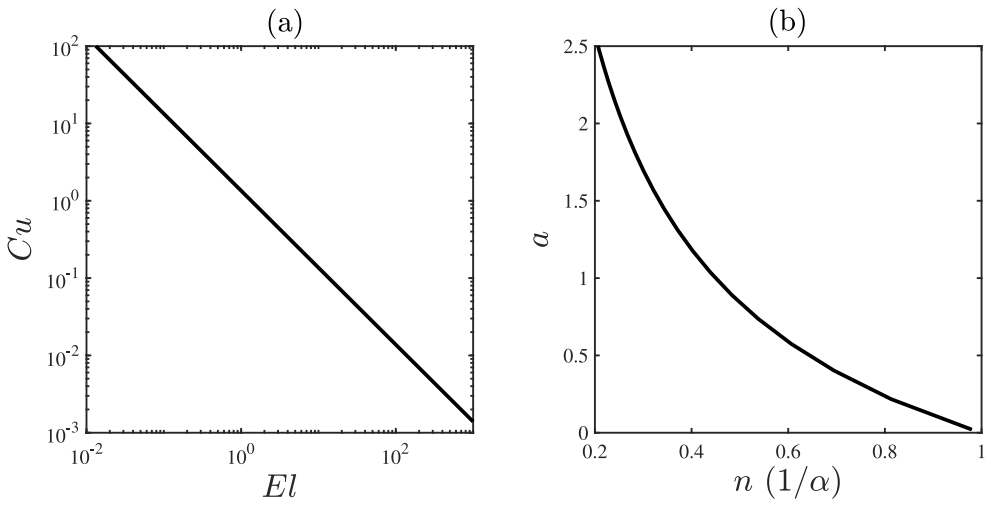

Fig. A.16. (a) Carreau number Cu vs the Ellis number, El; (b) The fitting parameter a in the Carreau viscosity model plotted as a function of the shear-thinning index n (or $(1/\alpha)$.

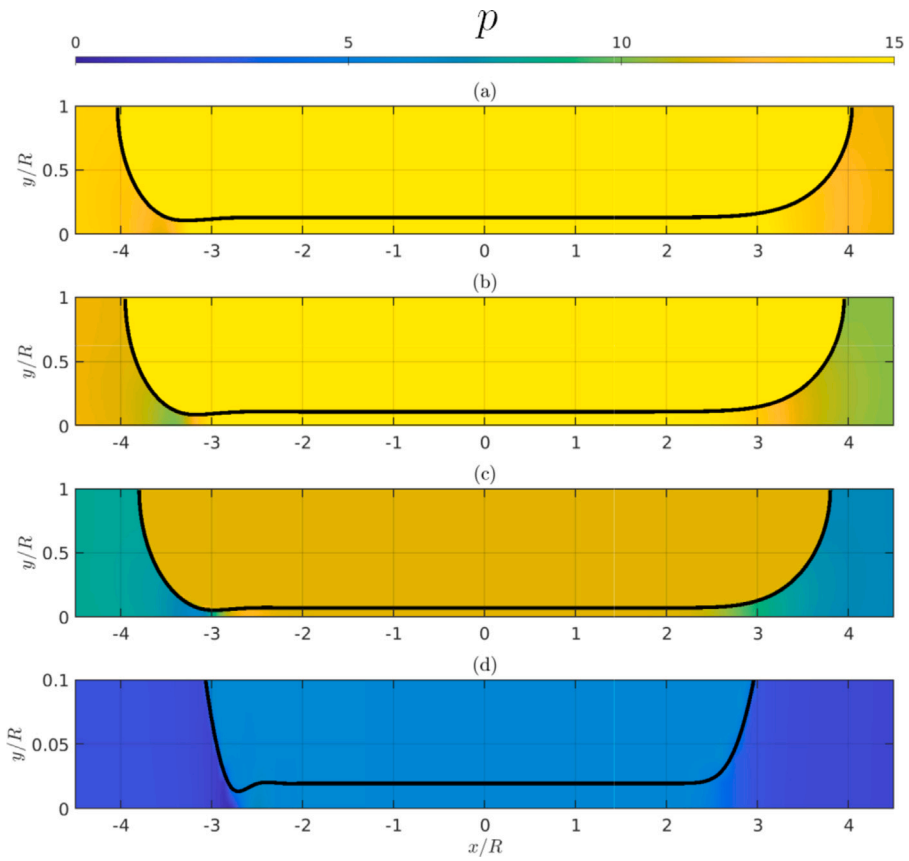

Fig. B.17. The pressure field in both the bubble and the shear-thinning liquid at $Ca_\infty = 0.05$, $n = 0.5$ and $a = 0.841$, while (a) $Cu^0_\infty = 2.5 \cdot 10^{-2}$, (b) $Cu^0_\infty = 2.5 \cdot 10^{-1}$, (c) $Cu^0_\infty = 2.5 \cdot 10^{0}$, (d) $Cu^0_\infty = 2.5 \cdot 10^{2}$.

maxima that corresponds to local minima of the effective viscosity. This effect is more pronounced at large Cu^0_∞, see Fig. 12(b)–(d).

Interestingly, the uniform film region is dominated by zero-shear-rate effects confirming that we can always identify a region of the bubble where the liquid exhibits a Newtonian behavior in the small Ca limit, see Picchi et al. [32]. In the uniform film, $\mu/\mu_0 \approx 1$ since the fluid is at rest. Far from the bubble, the effective viscosity can either approach again the Newtonian limit, Fig. 12(b), or approach a region dominated by the shear-thinning effect depending on the magnitude of the Carreau number, Fig. 12(d). Both these behaviors agree with the theoretical predictions of Picchi et al. [32]. The scenario changes while we approach finite capillary numbers, see Figs. 13, 14, and 15. Specifically, at a fixed Carreau number, the decrease in the effective viscosity in the bubble front and the rear becomes more pronounced. Although the film thickness increases with the capillary number, the uniform film region is still dominated by zero-shear-rate effects, except for extremely large Cu where the liquid is sheared enough to get a reduction of the effective viscosity, see Fig. 13(d). In regimes where $Ca_\infty = 1$ and $Cu^0_\infty \gg 1$ the uniform film is the less sheared region, suggesting that neglecting the zero-shear-rate behavior (for example, considering the power-law viscosity model) would lead to nonphysical results.

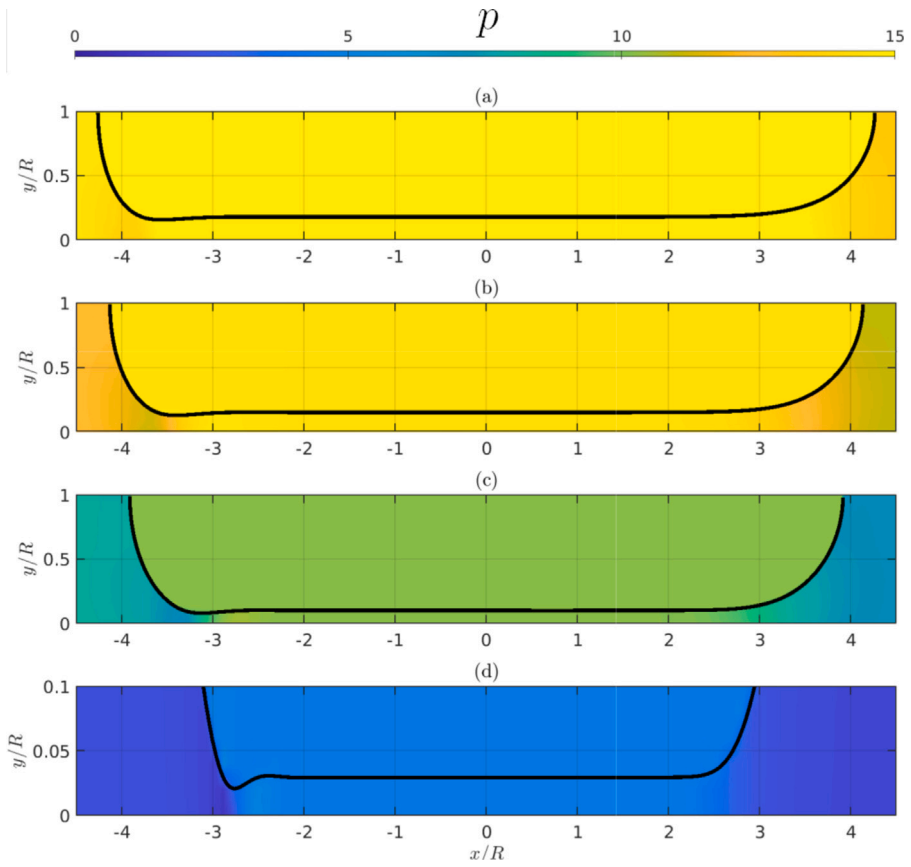

Fig. B.18. The pressure field in both the bubble and the shear-thinning liquid at $Ca_\infty = 0.1$, $n = 0.5$ and $a = 0.841$, while (a) $Cu^0_\infty = 2.5 \cdot 10^{-2}$, (b) $Cu^0_\infty = 2.5 \cdot 10^{-1}$, (c) $Cu^0_\infty = 2.5 \cdot 10^{0}$, (d) $Cu^0_\infty = 2.5 \cdot 10^{2}$.

In the bubble rear, the viscosity field reflects the typical oscillations of the meniscus. Specifically, the shape oscillations induce changes in the sign of the driving force leading to the formation of recirculating vortexes. The stagnant region between two adjacent vortexes corresponds to the spikes where the effective viscosity tends to approach unity. In correspondence of the vortex center, the shear is maximum and, therefore, the effective viscosity is minimum. This behavior is qualitatively consistent with the lubrication theory of Picchi et al. [32].

4. Conclusions

In this work, we studied the dynamics of Taylor bubbles which move in a shear-thinning fluid up to finite capillary numbers by means of numerical simulations. We focused on regimes where inertia and buoyancy can be neglected, investigating the effect of the fluid rheology on bubble characteristics (i.e., the film thickness, bubble speed, bubble shape, and the formation of recirculating patterns). The numerical simulations are carried out considering a shear-thinning fluid, whose viscosity follows the Carreau viscosity model, aimed at accounting for both zero-shear-rate and shear-thinning effects.

We show the existence of a general scaling law for the effective viscosity that allows the definition of the generalized capillary number of the problem. Specifically, the film thickness follows the two-third scaling law only when the effective capillary number is small (in agreement with the lubrication theory of Picchi et al. [32]). Otherwise, at finite capillary numbers, the film thickness saturates with the capillary number. To capture this behavior, we generalized the scaling law of Aussillous and Quéré [12] capturing the interplay between the zero-shear-rate and the shear-thinning effects. Also, starting from the mass balance, we derived a general scaling law for the bubble speed that applies up to finite capillary numbers.

The fluid rheology strongly influences the shape of the Taylor bubble. In particular, we quantify the interplay between the effect of the capillary number (which tends to increase the film thickness and elongates the bubble) and the shear-thinning effect, which tends to decrease the effective viscosity and, therefore, reduce the effective capillary number of the problem. The presence of recirculating vortexes ahead and behind the Taylor bubble and its location agrees well with the theory of Picchi et al. [32]. Interestingly, the uniform film region is dominated by zero-shear-rate effects confirming that we can always identify a region of the bubble where the liquid exhibits a Newtonian behavior while, in the bubble rear, the viscosity field reflects the typical oscillations of the meniscus.

Although the motivation of our work is oriented to understanding the dynamics of a single Taylor bubble, the scaling laws obtained may serve as a base to construct more sophisticated models for trains of bubbles.

CRediT authorship contribution statement

Andrea Aquino: Software, Formal analysis, Writing – original draft. **Davide Picchi:** Conceptualization, Formal analysis, Methodology, Writing – original draft, Writing – review & editing , Supervision. **Pietro Poesio:** Conceptualization, Writing – review & editing , Supervision.

Declaration of competing interest

The authors declare that they have no known competing financial interests or personal relationships that could have appeared to influence the work reported in this paper.

Data availability

Data will be made available on request.

Acknowledgment

We would like to thank Dr. Mirco Magnini (University of Nottingham) for useful and constructive discussions about the numerical setup.

Funding sources

This research did not receive any specific grant from funding agencies in the public, commercial, or not-for-profit sectors.

Appendix A. Correspondence between Carreau and Ellis viscosity models

Motivated by the fact that the theoretical model by Picchi et al. [32] is formulated in terms of Ellis viscosity model and the present simulations where done in terms of the Carreau viscosity model, here, we explain how the two models can be interchanged. Specifically, the Ellis viscosity model is given by

$$\mu = \frac{\mu_0}{1 + \left(\tau/\tau_{1/2}\right)^{\alpha-1}}, \tag{A.1}$$

where $n = 1/\alpha$ and $\tau_{1/2}$ is a parameter that controls the onset of the shear-thinning effect representing the effective shear stress at which the viscosity is 50% of the Newtonian limit.

Since the Carreau and the Ellis viscosity models have four and three fitting parameters, respectively, it is possible to fit the Carreau viscosity curve upon the Ellis one. Doing so, we get a correspondence between the two rheological models (in dimensionless coordinates)

$$\frac{\mu}{\mu_0} = [1 + (Cu\dot{\gamma})^a]^{\frac{n-1}{a}} \quad \longleftrightarrow \quad \frac{\mu}{\mu_0} = \frac{1}{1 + (\tau/El)^{\alpha-1}}, \tag{A.2}$$

where the Carreau and the Ellis numbers are defined based on a characteristic length $\mathcal{L}$ and a characteristic velocity $\mathcal{U}$ as

$$Cu = \frac{\lambda\,\mathcal{U}}{\mathcal{L}} \qquad El = \frac{\tau_{1/2}\,\mathcal{L}}{\mu_0\,\mathcal{U}}, \tag{A.3}$$

The shear-thinning index in the Carreau model is $n = 1/\alpha$ while Cu as function of El follows the evolution presented in Fig. A.16(a). Specifically, since Cu and $1/El$ acts as representative dimensionless shear rates, therefore, $Cu \sim El^{-1}$. This trend can be easily seen in the power-law limit where $Cu \gg 1$ and $El \ll 1$

$$\mu_{Carreau} \sim Cu^{n-1}\dot{\gamma}^{n-1} \qquad \mu_{Ellis} \sim El^{1-n}\dot{\gamma}^{n-1}. \tag{A.4}$$

The fitting parameter a in the Carreau viscosity model is a function of the shear-thinning index n as shown in Fig. A.16(b). Based on those plots it is always possible to find the correspondence between the Ellis and the Carreau viscosity models.

Appendix B. Pressure fields

Here, we present the pressure filled within the bubble and the shear-thinning liquid as a function of the Carreau number for $Ca_\infty = 0.05, 0.1$. Specifically, a pressure jump is maintained between the bubble tip and the surrounding liquid while, in the uniform film region, the pressure field is almost uniform, see Figs. B.17 and B.18.

References

[1] V. Ajaev, G. Homsy, Modeling shapes and dynamics of confined bubbles, Annu. Rev. Fluid Mech. 38 (1) (2006) 277–307.
[2] R. Chhabra, Bubbles, Drops, and Particles in Non-Newtonian Fluids, CRC Press, 2007.
[3] A.S. Lynn, Droplets and bubbles in microfluidic devices, Annu. Rev. Fluid Mech. 48 (1) (2016) 285–309.
[4] S. Khodaparast, M.K. Kim, J.E. Silpe, H.A. Stone, Bubble-driven detachment of bacteria from confined microgeometries, Environ. Sci. Technol. 51 (3) (2017) 1340–1347.
[5] J.L. Bull, Cardiovascular bubble dynamics, Crit. Rev. Biomed. Eng. 33 (4) (2005) 299–346.
[6] J. Grotberg, Pulmonary flow and transport phenomena, Annu. Rev. Fluid Mech. 26 (1) (1994) 529–571.
[7] A. Suzuki, D.M. Eckman, Embolism bubble adhesion force in excised perfused microvessels, Anesthesiology 99 (2003) 400–408.
[8] D.M. Eckmann, V.N. Lomivorotov, Microvascular gas embolization clearance following perfluorocarbon administration, J. Appl. Physiol. 94 (3) (2003) 860–868.
[9] F. Fairbrother, A.E. Stubbs, 119. Studies in electro-endosmosis. Part VI. The "bubble-tube" method of measurement, J. Chem. Soc. (Resumed) (1935) 527–529.
[10] G. Taylor, Deposition of a viscous fluid on the wall of a tube, J. Fluid Mech. 10 (2) (1961) 161–165.
[11] F.P. Bretherton, The motion of long bubbles in tubes, J. Fluid Mech. 10 (2) (1961) 166–188.
[12] P. Aussillous, D. Quéré, Quick deposition of a fluid on the wall of a tube, Phys. Fluids 12 (10) (2000) 2367–2371.
[13] B. Cox, On driving a viscous fluid out of a tube, J. Fluid Mech. 14 (1) (1962) 81–96.
[14] M. Heil, Finite Reynolds number effects in the Bretherton problem, Phys. Fluids 13 (9) (2001) 2517–2521.
[15] S. Khodaparast, M. Magnini, N. Borhani, J.R. Thome, Dynamics of isolated confined air bubbles in liquid flows through circular microchannels: an experimental and numerical study, Microfluid. Nanofluid. 19 (1) (2015) 209–234.
[16] M. Magnini, A. Ferrari, J. Thome, H.A. Stone, Undulations on the surface of elongated bubbles in confined gas-liquid flows, Phys. Rev. Fluids 2 (8) (2017) 084001.
[17] Y.E. Yu, L. Zhu, S. Shim, J. Eggers, H.A. Stone, Time-dependent motion of a confined bubble in a tube: transition between two steady states, J. Fluid Mech. 857 (2018).
[18] R. Bird, R. Armstrong, O. Hassager, Dynamics of Polymeric Liquids Vol 1: Fluid Mechanics, John Wiley and Sons Inc, United States, 1987.
[19] P.J. Carreau, Rheological equations from molecular network theories, Trans. Soc. Rheol. 16 (1) (1972) 99–127.
[20] K. Yasuda, R. Armstrong, R. Cohen, Shear flow properties of concentrated solutions of linear and star branched polystyrenes, Rheol. Acta 20 (1981) 163–178, http://dx.doi.org/10.1007/BF01513059.
[21] M. Reiner, Deformation, Strain, and Flow, Interscience, New York, 1965, p. 246.
[22] F. Kamişli, M.E. Ryan, Perturbation method in gas-assisted power-law fluid displacement in a circular tube and a rectangular channel, Chem. Eng. J. 75 (3) (1999) 167–176.
[23] F. Kamişli, M.E. Ryan, Gas-assisted non-Newtonian fluid displacement in circular tubes and noncircular channels, Chem. Eng. Sci. 56 (16) (2001) 4913–4928.
[24] D.A. de Sousa, E.J. Soares, R.S. de Queiroz, R.L. Thompson, Numerical investigation on gas-displacement of a shear-thinning liquid and a visco-plastic material in capillary tubes, J. Non-Newton. Fluid Mech. 144 (2) (2007) 149–159.
[25] R.L. Thompson, E.J. Soares, R.D. Bacchi, Further remarks on numerical investigation on gas displacement of a shear-thinning liquid and a visco-plastic material in capillary tubes, J. Non-Newton. Fluid Mech. 165 (7) (2010) 448–452.
[26] A. Kawahara, M. Sadatomi, W.Z. Law, M.H. Mansour, Characteristics of gas and non-newtonian liquid two-phase flows through a circular microchannel, Multiph. Sci. Technol. 27 (2–4) (2015).
[27] M. Fatehifar, A. Revell, M. Jabbari, Non-Newtonian droplet generation in a cross-junction microfluidic channel, Polymers 13 (2021).
[28] Q. Zhao, H. Ma, Y. Liu, C. Yao, L. Yang, G. Chen, Hydrodynamics and mass transfer of Taylor bubbles flowing in non-Newtonian fluids in a microchannel, Chem. Eng. Sci. 231 (2021) 116299.
[29] D. Picchi, A. Ullmann, N. Brauner, Modeling of core-annular and plug flows of Newtonian/non-Newtonian shear-thinning fluids in pipes and capillary tubes, Int. J. Multiph. Flow. 103 (2018) 43–60.
[30] D. Picchi, I. Barmak, A. Ullmann, N. Brauner, Stability of stratified two-phase channel flows of Newtonian/non-Newtonian shear-thinning fluids, Int. J. Multiph. Flow. 99 (2018) 111–131.
[31] R. Hewson, N. Kapur, P. Gaskell, A model for film-forming with Newtonian and shear-thinning fluids, J. Non-Newton. Fluid Mech. 162 (1–3) (2009) 21–28.
[32] D. Picchi, A. Ullmann, N. Brauner, P. Poesio, Motion of a confined bubble in a shear-thinning liquid, J. Fluid Mech. 918 (2021).

[33] A.I. Moreira, L.A. Rocha, J. Carneiro, J.D. Araújo, J.B. Campos, J.M. Miranda, Isolated taylor bubbles in co-current with shear thinning cmc solutions in microchannels—A numerical study, Processes 8 (2) (2020) 242.
[34] S.G. Sontti, A. Atta, CFD study on Taylor bubble characteristics in Carreau-Yasuda shear thinning liquids, Can. J. Chem. Eng. 97 (2) (2019) 616–624.
[35] R. Sousa, M. Riethmuller, A. Pinto, J. Campos, Flow around individual Taylor bubbles rising in stagnant CMC solutions: PIV measurements, Chem. Eng. Sci. 60 (7) (2005) 1859–1873, http://dx.doi.org/10.1016/j.ces.2004.11.035, URL: https://www.sciencedirect.com/science/article/pii/S0009250904009431.
[36] H. Scheufler, J. Roenby, Accurate and efficient surface reconstruction from volume fraction data on general meshes, J. Comput. Phys. 383 (2019) 1–23.
[37] G. Tryggvason, R. Scardovelli, S. Zaleski, Direct Numerical Simulations of Gas–Liquid Multiphase Flows, Cambridge University Press, 2011.
[38] M. Rudman, A volume-tracking method for incompressible multifluid flows with large density variations, Internat. J. Numer. Methods Fluids 28 (2) (1998) 357–378.
[39] L. Gamet, M. Scala, J. Roenby, H. Scheufler, J.-L. Pierson, Validation of volume-of-fluid openFOAM® isoadvector solvers using single bubble benchmarks, Comput. & Fluids 213 (2020) 104722.
[40] J.U. Brackbill, D.B. Kothe, C. Zemach, A continuum method for modeling surface tension, J. Comput. Phys. 100 (2) (1992) 335–354.
[41] S.B. Lee, A study on temporal accuracy of openFOAM, Int. J. Nav. Archit. Ocean Eng. 9 (4) (2017) 429–438.
[42] M.F. Silva, J.B. Campos, J.M. Miranda, J.D. Araújo, Numerical study of single taylor bubble movement through a microchannel using different CFD packages, Processes 8 (11) (2020) 1418.
[43] B. Van Leer, Towards the ultimate conservative difference scheme. II. Monotonicity and conservation combined in a second-order scheme, J. Comput. Phys. 14 (4) (1974) 361–370.
[44] D.A. Hoang, V. van Steijn, L.M. Portela, M.T. Kreutzer, C.R. Kleijn, Benchmark numerical simulations of segmented two-phase flows in microchannels using the volume of fluid method, Comput. & Fluids 86 (2013) 28–36.
[45] G. Balestra, L. Zhu, F. Gallaire, Viscous Taylor droplets in axisymmetric and planar tubes: from Bretherton's theory to empirical models, Microfluid. Nanofluid. 22 (6) (2018) 1–27.
[46] P.W. Holland, R.E. Welsch, Robust regression using iteratively reweighted least-squares, Comm. Statist. Theory Methods 6 (9) (1977) 813–827, http://dx.doi.org/10.1080/03610927708827533.